Materials
Horizons

COMMUNICATION

View Article Online
View Journal

Check for updates

Cite this: DOI: 10.1039/d6mh00281a

Received 13th February 2026,
Accepted 29th April 2026

DOI: 10.1039/d6mh00281a

rsc.li/materials-horizons

Time–temperature–transformation-layering diagrams: a design tool for lightweight multi-layered, single-material polymeric structures

Emilia Di Lorenzo, †[ab] Lorenzo Miele, †[ab] Alessandra Longo, *[c]
Ernesto Di Maio *[ab] and Maria Laura Di Lorenzo [c]

In the design for recycling strategy, reducing the number of different materials is encouraged. However, multi-material structures like multi-layers are often used to optimize performance. Here, we demonstrate that, by engineering the coupled mass and heat transport during the processing of semi-crystalline polymeric components, it is possible to achieve a multilayered structure using a single material. Layering—in terms of crystallinity and foaming—has been accomplished by identifying the processing window in which the characteristic times are of the same order of magnitude for (i) mass transport of the foaming agent, (ii) heat transport and (iii) polymer crystallization. A time–temperature–transformation-layering diagram is thus constructed and exploited. This strategy has been validated using two different semi-crystalline polymers, poly(lactic acid) and poly(ethylene terephthalate), and CO_2 as a foaming agent. We demonstrate that sustainability and performance need not be mutually exclusive. Possibility of leveraging this approach with other types of materials and/or processes for which layering is required significantly broadens the scope of this research.

New concepts

This work introduces a framework for designing mono-material, multi-layered structures within a single component, eliminating the need for melt bonding, soldering, or adhesives while enhancing performance, sustainability, and manufacturing simplicity. The central advance lies in redefining time–temperature–transformation (TTT) diagrams, which traditionally describe transformation kinetics under spatially uniform conditions and provide no guidance for spatial structuring. Here, transport bands are superimposed onto TTT diagrams to incorporate the characteristic length and time scales of heat and/or mass transport, identifying regions where transport rates are comparable to transformation kinetics over a defined depth. This transforms the classical TTT diagram into a spatio-temporal design map that enables the deliberate formation of layered architectures within a single material. Polymers serve as model systems, with poly(lactic acid) and poly(ethylene terephthalate) subjected to combined pressurized carbon dioxide and thermal treatments, producing controlled variations in structure and density from initially amorphous samples in a single processing step. More broadly, the framework establishes a generalizable principle for coupling transport phenomena with phase transformation kinetics, offering a versatile conceptual tool for research and materials engineering education.

1 Introduction

Material layering is a prevalent strategy for optimizing structural and functional performance and is commonly observed in both natural and artificial systems.[1–3] From a structural perspective, layering is often employed to address the conflict between strength and toughness, as these are equally vital requirements; however, they are generally mutually exclusive.[4] Sandwich structures, formed by a low-density core—in some cases a foam—and high-stiffness, fiber-reinforced composite outer layers, are examples of this nature-mimicking, performance-improving strategy, and are found in advanced applications such as wind turbines, boats, and aircraft.[5] From a functional perspective, multilayer structures are utilized in electronics, electromagnetic shielding, sensing, packaging, energy, medicine, pharmaceuticals, *etc.* However, in functional applications, the necessity for an active layer and the high added value of typical products may limit the relevance of the present study.

The intimate bonding of different materials in multi-layer systems makes their recycling, both mechanical and chemical, extremely challenging. Within the design for recycling approach, mono-material systems are strongly preferred over

---

[a] *Dipartimento di Ingegneria Chimica, dei Materiali e della Produzione Industriale, University of Naples Federico II, Piazzale Vincenzo Tecchio, 80, Naples 80125, Italy. E-mail: edimaio@unina.it*
[b] *foamlab, University of Naples Federico II, Piazzale Vincenzo Tecchio, 80, Naples 80125, Italy*
[c] *National Research Council, Institute of Polymers, Composites and Biomaterials, Via Campi Flegrei, 34, Pozzuoli (NA) 80078, Italy. E-mail: alessandra-longo@cnr.it*

† These authors contributed equally to this work.

multi-material ones.[6–8] In mono-material layered systems, different properties can be achieved through variations in composition and structure (*e.g.*, orientation and crystallinity), and fine-tuning of additives (*e.g.*, 2D materials to enhance barrier properties in packaging).[9] The search for suitable material solution is currently vibrant and diverse, with innovative and creative strategies aimed at matching the performance of multi-material systems.[10–12] However, from a processing standpoint, comparable effort appears to be lacking in the development of simplified technologies that address the need for improved sustainability and recyclability of products.

In this context, some of the authors introduced the concept of time-varying boundary conditions in (i) mass and (ii) heat transport problems during processing to achieve layering. These were applied respectively to (1) polymer foaming[13] and (2) egg cooking.[14,15] In particular, in ref. 13, multi-graded foams were obtained by imposing a pressure treatment with a characteristic time t_p on the order of the mass transport characteristic time, $\tau_\mathrm{m} = L^2/D$, where L is the characteristic size of the part and D is the mutual diffusivity of the polymer/foaming agent system. This pressure treatment induces a non-equilibrium foaming agent concentration profile, $c = c(x,t)$. Upon an instantaneous pressure release (*i.e.*, with a characteristic time $t_\mathrm{f} \ll t_\mathrm{p}$) at a given time $\bar{t}$, foaming is achieved. In some sense, the pressure release "writes" the concentration profile $c = c(x,\bar{t})$. Notably, the resulting foam exhibits a lower density and a higher bubble number density in regions (x) where c is larger.

In ref. 14, the same concept was applied to induce layering in eggs, allowing for the cooking of the albumen and the yolk at two different temperatures (the optimal cooking temperatures are 65 °C for the yolk and 85 °C for the albumen). Again, by using a temperature treatment with a characteristic time t_T on the order of the heat transport characteristic time, $\tau_\mathrm{h} = L^2/a$, where a is the thermal diffusivity of the albumen, a non-equilibrium temperature profile $T = T(x,t)$ is induced. Unlike the previous case, in cooking (as well as in other temperature treatments that induce material changes, such as curing or crystallization in polymers), the instantaneous temperature profile $T = T(x,\bar{t})$ is not sufficient to establish a cooking degree profile, as cooking requires time. A characteristic time can be defined here, for example, as the half-time of the cooking reaction to completion, $\tau_X(T) = 1/k$, where k is the reaction kinetics constant. Time integration of the reaction kinetics yields the degree of cooking. In this case, as the temperature profile evolves over time, one must be inventive in designing temperature treatments that meet the desired objectives. In ref. 14, the authors introduced periodic cooking as the treatment to fully cook the yolk and albumen, where a number N of high-temperature and low-temperature cooking cycles were applied, with $N = \tau_X/\tau_\mathrm{h}$.

The concurrent use of the two aforementioned transport phenomena is employed here to induce layering in both the density and the degree of crystallinity in slabs of two model polymers: poly(lactic acid) (PLLA) and poly(ethylene terephthalate) (PET). Mono-material, multi-layered parts are thus designed and processed in a single step during pressure release, following a well-defined heat and pressure treatment.

We therefore demonstrate how knowledge of the combined interaction of transport phenomena and phase transformations during material processing allows for an accurate, unprecedented prediction of the final morphology. A graphic tool, the time, temperature, transformation, and layering – TTTL – map, is proposed to visualize the idea and verify the available processing window to achieve the desired layered structure. Possible extensions to any material and treatment type are suggested and encouraged.

2 Materials and methods

2.1 Materials

Amorphous PLLA grade Lx175, with a melt flow index (210 °C/2.16 kg) of 6 and 4% D-isomer units, was kindly provided by Total Corbion (Gorinchem, The Netherlands). PET M4 P80 was kindly received from PointPlastic S.r.l. (Amasona, Italy).

The PLLA and the PET were first dried at 60 °C under vacuum overnight and then shaped into sheets of 2.0 and 1.5 mm thickness, respectively, *via* compression molding, followed by rapid quenching to ambient temperature to hinder crystals formation. In both cases, disks of 5 mm diameter were formed by punching the sheets. In the case of PLLA, slabs ($18 \times 2 \times 100$ mm^3 in dimensions) were also cut out from the sheets for three point bending tests.

CO_2 (purity 99.99%) was purchased from SOL S.p.A. (Monza, Italy).

2.2 Methods

2.2.1 Physical foaming experiments. Physical foaming of the PLLA and PET slabs in the shape of disks was performed in a custom-made pressure vessel, thoroughly described elsewhere,[16,17] designed to allow the fine-tuning of all the foaming parameters (temperature, pressure, and pressure drop rate (PDR)). Before the actual experiment, the vessel was preheated to the desired temperature to prevent possible effects of the heating ramp on the polymer microstructure build-up (*i.e.*, cold crystallization). Once the desired temperature was reached (ranging from 45 to 120 °C in the case of PLLA and from 70 to 260 °C in the case of PET), the foaming experiment was initiated by loading one PLLA (or PET) disk into the vessel and subsequently increasing the pressure up to 110 bar of CO_2. The lower temperature limit of the processing window is related to the glass transition temperature (T_g), which is T_g = 60 °C for PLLA[18] and T_g = 69 °C for PET,[19] without taking into account the plasticizing effect of CO_2.[18,20] The upper temperature relates to the melting points of the two polymers, as quantified in ref. 21–24 for PLLA, and in ref. 19 for PET.

The pressure was then maintained at a constant value for a time of t_p = 2, 5, 10, 20, and 40 min in the case of PLLA and for t_p = 2 and 30 min in the case of PET. Finally, the pressure was rapidly released over a time period of $t_\mathrm{f} \ll t_\mathrm{p}$, and the foamed sample was removed from the reactor and stored at room temperature. In the case of PET, a non-isothermal treatment was also attempted, involving (i) loading the sample into the pre-heated pressure vessel at $T = 260$ °C, (ii) increasing the CO_2 pressure up to 110 bar, and (iii) continuous cooling the pressure vessel down to 220 °C over a time span of 8 min before pressure quenching. For the PLLA slabs, the same foaming procedure was followed, but a pressure vessel characterized by a larger internal volume was used, as fully detailed in ref. 25.

2.2.2 Microscopy. The foamed samples were extracted from the vessel and characterized in terms of morphology by optical microscopy. The treated samples were cut in half using an ultra-thin stainless steel blade, and their morphology was observed using an optical microscope (Stemi 508, Zeiss, Oberkochen, Germany). The thickness of each visible layer in the cross section was quantified using the ImageJ software (in the best case, this included a crystalline skin, a foamed part, and the unfoamed core of the sample). The thickness of the saturated layer (x) was determined by evaluating the difference between the initial thickness of the sample and the core thickness. From this, the polymer/foaming agent (hereafter referred to as gas) mutual diffusivity at different temperatures was estimated as follows:

$$D \approx \frac{x^2}{t_\mathrm{p}} \tag{1}$$

This procedure was followed equally for PLLA and PET, allowing us to retrieve the light red diamonds shown in Fig. 1 and 6. In fact, even minor variations in material characteristics, such as molecular weight polydispersity, can result in significant differences in the physical properties of the polymer. Therefore, for accurate and quantitative processing design, specific material analysis is required.

On the other side, the treated samples were also analyzed with a Zeiss Axioskop polarized optical microscope (POM), equipped with a CFW-1312C Digital Camera (Scion Corporation, Maryland, USA). Images were captured with Image-Pro Plus 7.0 software (Media Cybernetics). The foams were embedded in resin and cut, parallel to the direction of the characteristic length, into 30 μm thick slices by means of a cryomicrotome (Olympus DP 21, Tokyo, Japan) at −20 °C.

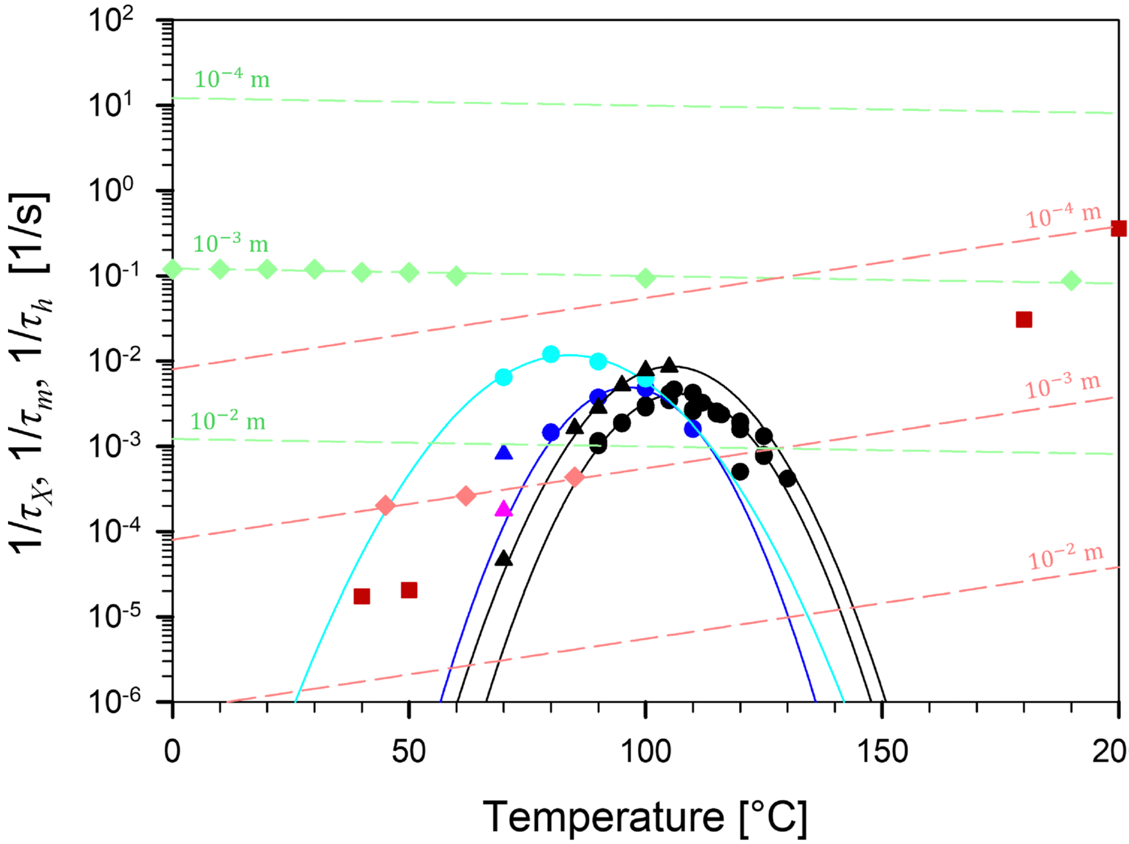

Fig. 1 Comparison of the rates of the three concurring phenomena for the system PLLA/CO_2. $1/\tau_m = D/L^2$ is the rate of mass transport (full dark red squares were taken from Refs.,[26–29] while light red diamonds are our data); $1/\tau_h = a/L^2$ (green diamonds) is the rate of heat transport;[30] $1/\tau_X$ is the crystallization rate, evaluated as the reciprocal of the half-time of crystallization. The latter is presented as a function of CO_2 pressure: black, blue and cyan circles indicate $1/\tau_X$ at ambient pressure,[31–34] with 15 bar of CO_2[31] and with 45 bar of CO_2,[31] respectively, in the case of melt crystallization; similarly, black, pink and blue triangles indicate $1/\tau_X$ at ambient pressure,[33,35] with 5 bar of CO_2[35] and with 20 bar of CO_2[35] in the case of cold crystallization. Values of L = 0.1, 1 and 10 mm were used for the evaluation of $1/\tau_m$ (red dashed lines) and $1/\tau_h$ (green dashed lines). Continuous crystallization lines are used as a guide to the eye. In all cited references, PLLA has a D-isomer content of 4% and a molecular weight ranging between 40 and 200 kDa.

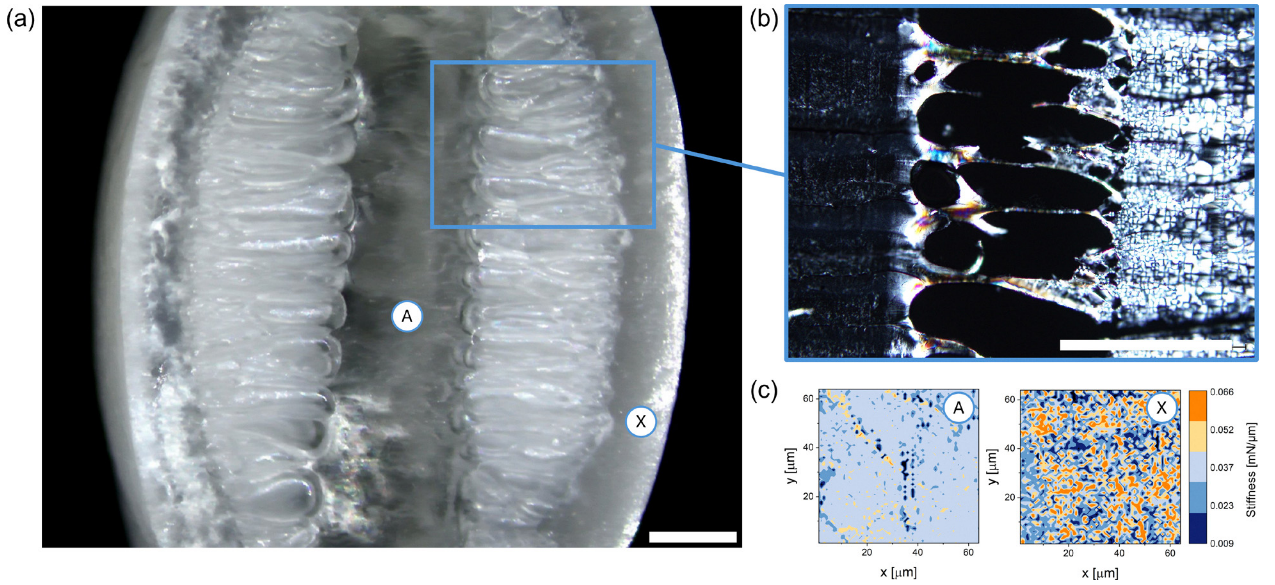

Fig. 2 (a) Optical microscopy image of a cross section of a PLLA sample treated at high pressure of CO_2; (b) cross-polarized optical micrograph of a 30 μm thick slice of PLLA in the transition region from the core to skin, and (c) AFM stiffness mapping in a 64 × 64 μm region in the core (A) and the skin (X) of the foamed PLLA sample. Scale bar = 500 μm in both (a) and (b).

The resulting slices were placed on glass slides and carefully washed with water to remove the resin before POM imaging. This procedure was only followed for PLLA.

2.2.3 Thermal analysis. The thermal properties and crystallization kinetics of the samples were investigated using a PerkinElmer (Massachusetts, United States) pyris diamond differential scanning calorimeter (DSC), equipped with an intracooler II as a cooling system, in isothermal mode by varying the cold crystallization temperature. Temperature and energy calibration were performed with a high purity indium standard. Dry nitrogen gas was used to purge the sample environment at a flow rate of 30 mL min^{-1}. All experiments were repeated three times to ensure reproducibility. Each heating scan was performed from 0 to 200 °C at a rate of 20 °C min^{-1}. To obtain accurate heat capacity data from the heat flow rate measurements, each scan was paired with a reference run using an empty pan, with the masses of the aluminum sample pan and the reference pan matched within 0.03 mg. More details are presented in ref. 36.

2.2.4 Atomic force microscopy. Stiffness mapping of the three-layered PLLA slabs was performed using atomic force microscopy (AFM); a PLLA foamed sample was cut into a sub-millimeter thick slice with an ultra-thin stainless steel blade. An inverted optical microscope (Olympus IX71, Tokyo, Japan) equipped with a 10× objective (Olympus PLN 10×, Tokyo, Japan) was integrated with an AFM instrument (NTMDT NTEGRA Prima, Sutton, The Netherlands) to position the AFM head directly on top of the optical microscope, thereby allowing observation of the slab during the testing procedures.[37] A silicone probe with a nominal cantilever spring constant ranging between 0.01 and 0.5 N m^{-1} (CSG10, TipsNano, Tallinn, Estonia) was used for mapping stiffness in contact mode over an area of 64 × 64 μm both in the core and the outer layer of the sample.

2.2.5 Three-points bending tests. Bending tests were carried out in a three-point bending configuration using the MTS Alliance RT/50 (Eden Prairie, Minnesota, USA) universal testing machine equipped with a load cell of 50 kN. The span was fixed at 50 mm, and a displacement rate of 5.0 mm min^{-1} was adopted. For each sample, three specimens were manufactured and tested. The bending stiffness was evaluated as the initial slope of the force–displacement curve, and the fracture energy was determined as the area beneath the entire curve. All samples had the same initial weight.

3 Results

Literature data[26–35] on the effect of temperature on thermal and mass diffusivities, as well as on crystallization under CO_2 for PLLA, can be compared to infer the possibility of designing treatments that induce the formation of layers endowed with different degrees of crystallinity and/or foaming. These data were collected and processed to derive the characteristic times of mass and heat transport and of crystallization (τ_m, τ_h, and τ_X, as defined in the Introduction). Characteristic dimensions spanning three orders of magnitude (L = 0.1, 1 and 10 mm) were considered for the calculation. The corresponding rates of mass and heat transport and of crystallization were then derived as the respective reciprocals ($1/\tau_m$, $1/\tau_h$, and $1/\tau_X$), and their comparison is shown in Fig. 1, which reports data referring to PLLA grades containing 4% of D-isomer with molar weight ranging between 40 and 200 kDa. The latter range was selected based on literature knowledge on the influence of main parameters (molecular weight, melt flow index, and stereoregularity) on crystallization of PLLA.[38–41] Moreover, we considered overall crystallization rates, which take into account both crystal nucleation and growth rates, for various CO_2 pressure, due to its huge effect on crystallization of PLLA.[20]

As can be seen, the rate of heat transport is relatively constant in the reported experimental range, while the rate of mass transport increases exponentially with temperature, as typically reported in the literature. The crystallization rate, on the other hand, exhibits non-monotonic behavior with temperature, showing the characteristic bell shape,[23] and is massively affected by sorption of high pressure CO_2,[18,31,35,42,43] due to the CO_2 plasticization effect.[44] Indeed, the dissolved gas increases the mobility of the polymer chains and, consequently, it determines an increase in the rate of crystallization.[45] This behavior is evident from the blue, cyan, and pink data in Fig. 1,[31] showing that the crystallization rate peak not only increases but also shifts towards lower temperature values as the CO_2 pressure is progressively increased, and this is valid for both cold and melt crystallization.

The shift, which is here shown up to 45 bar of CO_2, is expected to be enhanced at higher pressures, compatibly with the increased amount of gas sorbed.[45] This will be taken into account later in this article to allow for validation of the experimental campaign conducted at 110 bar. In the general case of lack of data in the literature, this shift can be assessed relying on well-estabilished theoretical predictions.[46–48] Fig. 1 guides the design of treatments to achieve structure and density layering: once the characteristic dimension of the sample of interest is known, the user can leverage the direct comparison between the occurring phenomena to understand the appropriate processing conditions for this purpose. In the case of a 2 mm slab of PLLA (L = 1 mm), the high rate of heat transport (green lines) hinders the use of thermal treatments as a means to induce material structure layering, since the temperature quickly equilibrates within the given sample (temperature can be considered uniform). The design of the process may then be restricted to the sole exploitation of polymer crystallization and CO_2 diffusion, which show comparable rates in the temperature range of 40 to 140 °C, where structure and density layering becomes feasible. To validate this approach, a batch foaming experiment was conducted at 45 °C. A slab of amorphous PLLA (L = 1 mm) was treated with 110 bar of CO_2 for t_p = 20 min, and then pressure quenched with t_f = 0.1 s for foaming.

The optical microscopy image of the cross-section of the resulting sample is presented in Fig. 2a. A multilayer structure can be recognized: as we move from the skin towards the core of the sample, we encounter, in sequence, a dense layer, a foamed layer, and another dense, compact layer in the exact center of the slab. The thermal analysis (differential scanning calorimetry), as fully detailed in ref. 36, reveals the nature of the dense layers, indicating a difference in the degree of crystallinity, which is 0.23 for the outer layer and 0.02 for the central layer. This difference is also confirmed by the POM micrograph shown in Fig. 2b, which reveals the presence of round, bright elements, typical of spherulite formations, in the outer layer, but not in the core, which remains dark: optical isotropy is evidenced here, as characteristic of amorphous material.[49,50] AFM stiffness mapping (Fig. 2c) also confirms the physical state of the two layers. A uniform stiffness value of approximately 0.037 mN μm^{-1} is measured in the amorphous area (A), while a bimodal distribution of stiffness values is detected in the outer layer (X), with the modes being 0.023 and 0.057 mN μm^{-1}, again evidencing the presence of stiff crystalline domains within a soft amorphous matrix.[51–53]

This result is fully compatible with expectations arising from the qualitative analysis of Fig. 1. When the amorphous PLLA slab is placed in the autoclave at 45 °C, the crystallization rate is uniformly negligible (the black curve lies above 45 °C). As the sample comes into contact with CO_2 during pressurization, the gas diffuses into the system at a rate of $1/\tau_m > 1/\tau_X$. However, as the gas penetrates the PLLA slab, the crystallization rate curve increases locally (cyan curve), and $1/\tau_X$ begins to approach $1/\tau_m$.[45] As a consequence, a front of crystallinity appears, which lags behind the diffusive front of CO_2 penetrating inside the polymer. At pressure quench, we are able to freeze these two chasing fronts: within the CO_2 penetration depth, only the non-crystallized layer is allowed to expand, and if the front has not passed through the whole sample, the presence of three different layers is highlighted, just as previously described: an amorphous core, a foamed layer, and a crystalline skin.

This successful experiment confirms the possibility of exploiting Fig. 1 as a source of information for material and process design. Indeed, Fig. 1 can be used as a starting point to obtain a proper time–temperature–transformation–layering (TTTL) diagram that the user can leverage as a guide to understand the interplay between the concurrent phenomena occurring inside the sample and, consequently, to predict the resulting sample morphology. The TTTL diagram for a slab of PLLA with L = 1 mm, in which a layering with a characteristic dimension δ of 0.1 mm is desired, is fully shown in Fig. 3a. Here, consistent with the quick heat transport, we omitted the corresponding curves.

Concerning the rate of gas diffusion ($1/\tau_m$), two lines were selected: the first one ($1/\tau_m^{\delta}$) was evaluated considering δ = 0.1 mm, while the second one ($1/\tau_m^{L}$) was evaluated considering L = 1 mm. These two lines together approximately mark the beginning and end of the diffusion phenomenon in the sample. The bell-shaped curves of the crystallization rate of PLLA in the absence of CO_2 and in the presence of CO_2 (at the pressure value corresponding to the desired experimental condition) delineate the pink areas. The latter evidence the regions in which crystallization is allowed to occur, either at ambient or high pressure, and are specifically modified to better depict their interaction with gas diffusion. An additional bell-shaped curve is also represented, just below $1/\tau_m^{L}$, as an indicator of crystallization when the processing time t_p is long enough to fully crystallize the sample. Superimposition of the modified kinetic curves, in coherence with the presented discussion, highlights the presence of six different regions: given the processing conditions (temperature and time), the final sample can result in being fully amorphous (A), fully crystalline (X), fully foamed (F), or, as in the previously reported case, layered;

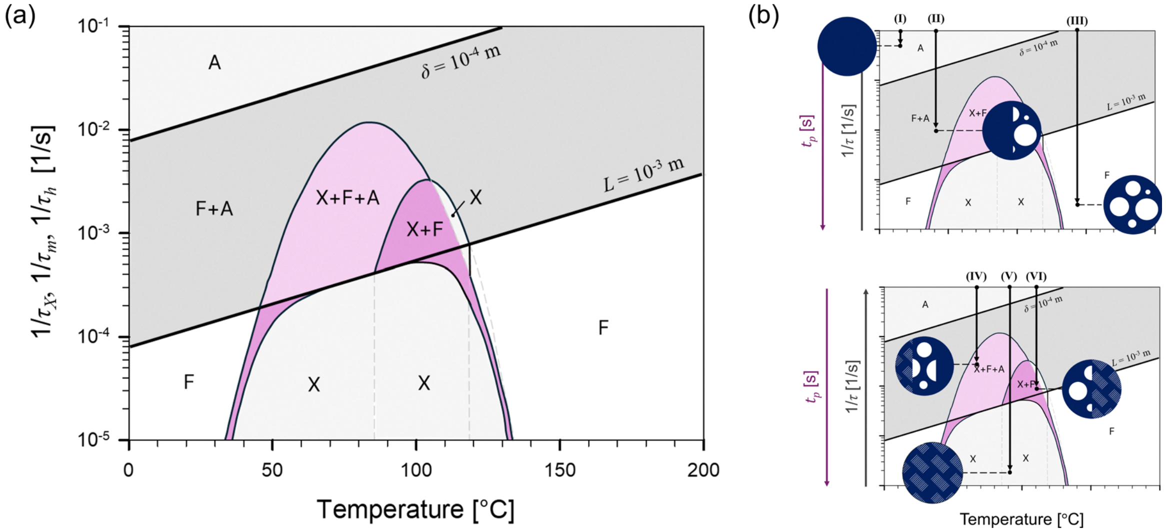

Fig. 3 (a) TTTL diagram for a slab of PLLA (L = 1 mm) treated with CO_2. The superimposition of the kinetic curves evidences the presence of six different regions that can help understanding the processing conditions required to obtain a certain morphology: amorphous (A, light grey), crystalline (X, grey), foamed (F, white), two-layered foamed–amorphous structure (F + A, dark grey), two-layered foamed–crystalline structure (X + F, dark pink) and three-layered foamed–amorphous–crystalline structure (X + F + A, pink). (b) Example of how thermal treatments can be displayed in the TTTL diagram.

i.e., a combination of the aforementioned (either F + A, X + F, or X + F + A). In other words, layering only arises when the system undergoes transformation under non-uniform chemical potential fields.

In order to generalize the concept, the possibility for inducing layering can be rapidly assessed using the Damköhler number ($\mathrm{Da} = \tau_\mathrm{m}/\tau_\mathrm{X}$), directly relating the transformation rate to the transport rate, specifically in the region in which layering is desired (δ). Given the processing conditions (time, temperature and thickness), only when $\mathrm{Da}_\delta \approx 1$ layering arises.

To better understand the potential of this diagram in the laboratory or industrial practice of batch foaming, a series of case studies is also presented (Fig. 3b). Here, on each TTTL diagram, the duration of the treatment is depicted as an arrow: when the arrow crosses a kinetic curve, the corresponding transformation occurs inside the system; the final sample morphology is determined by the final region reached by the arrow.

In case (I), the arrow does not cross any kinetic curve and remains confined in region (A), meaning that no transformation occurs and the sample stays amorphous; this happens at any temperature when $t_\mathrm{p} < \tau_\mathrm{m}^\delta$.

In case (II), the arrow only crosses the first diffusion curve but not the second one or any crystallization curve, reaching the (F + A) region; this occurs when $\tau_\mathrm{m}^\delta < t_\mathrm{p} < \tau_\mathrm{m}^L$ and, if in the temperature range where crystallization is enabled ($45 < T < 120$ °C), $t_\mathrm{p} > \tau_X$. In this instance, the temperature does not favor crystallization, and the processing time is long enough to allow diffusion in just a portion of the sample, which, upon pressure release, results in only partial foaming.

In case (III), the arrow crosses both the diffusion curves but not the crystallization curves, reaching the (F) region; this occurs when $t_\mathrm{p} > \tau_\mathrm{m}^L$ and the temperature does not enable sample crystallization ($T < 35$ °C or $T > 135$ °C, approximately). In this instance, the final sample, upon pressure quenching and thanks to gas uptake, is fully foamed.

Case (IV) is the most interesting one. Here, the arrow crosses both the first diffusion curve and the high pressure crystallization curve, reaching the (X + F + A) region. This can only happen when $t_\mathrm{p} > \tau_\mathrm{m}^\delta$ and $t_\mathrm{p} > \tau_X$, given that the temperature is sufficient to activate CO_2-induced crystallization (again $45 < T < 120$ °C). As a consequence, the portion of the sample that is not reached by the gas remains amorphous, while the other portion undergoes gas-induced crystallization in the form of a front lagging behind the diffusion front. Overall, upon pressure release, a three-layered structure is formed, with an amorphous core, a foamed part, and a crystalline skin. The example presented in Fig. 2 fits into this case.

In case (V), the arrow not only crosses the diffusion curves but also the crystallization curves, falling in the (X) region. This happens when $t_\mathrm{p} > \tau_\mathrm{m}^L$ in the temperature range where crystallization is allowed, whether simple or gas-induced. The combination of such temperatures and processing times allows for thorough crystal formation, and the final sample is fully crystalline.

Finally, case (VI) shows intermediate behavior between case (IV) and case (V). Here, the arrow crosses the first diffusion curve and both crystallization curves (*i.e.*, temperature favors crystallization and, concomitantly, $\tau_\mathrm{m}^\delta < t_\mathrm{p} < \tau_\mathrm{m}^L$), reaching region (X + F). Accordingly, the portion of the sample reached by the gas undergoes gas-induced crystallization (with a crystallization front lagging behind the diffusion front), while the other portion, differing from case (IV), fully crystallizes, being in the region where crystallization without CO_2 is also promoted. The final morphology features a two-layered structure, with a foamed part surrounded by crystals.

An experimental campaign aimed at validating the TTTL diagram was conducted on slabs of PLLA (L = 1 mm). The explored

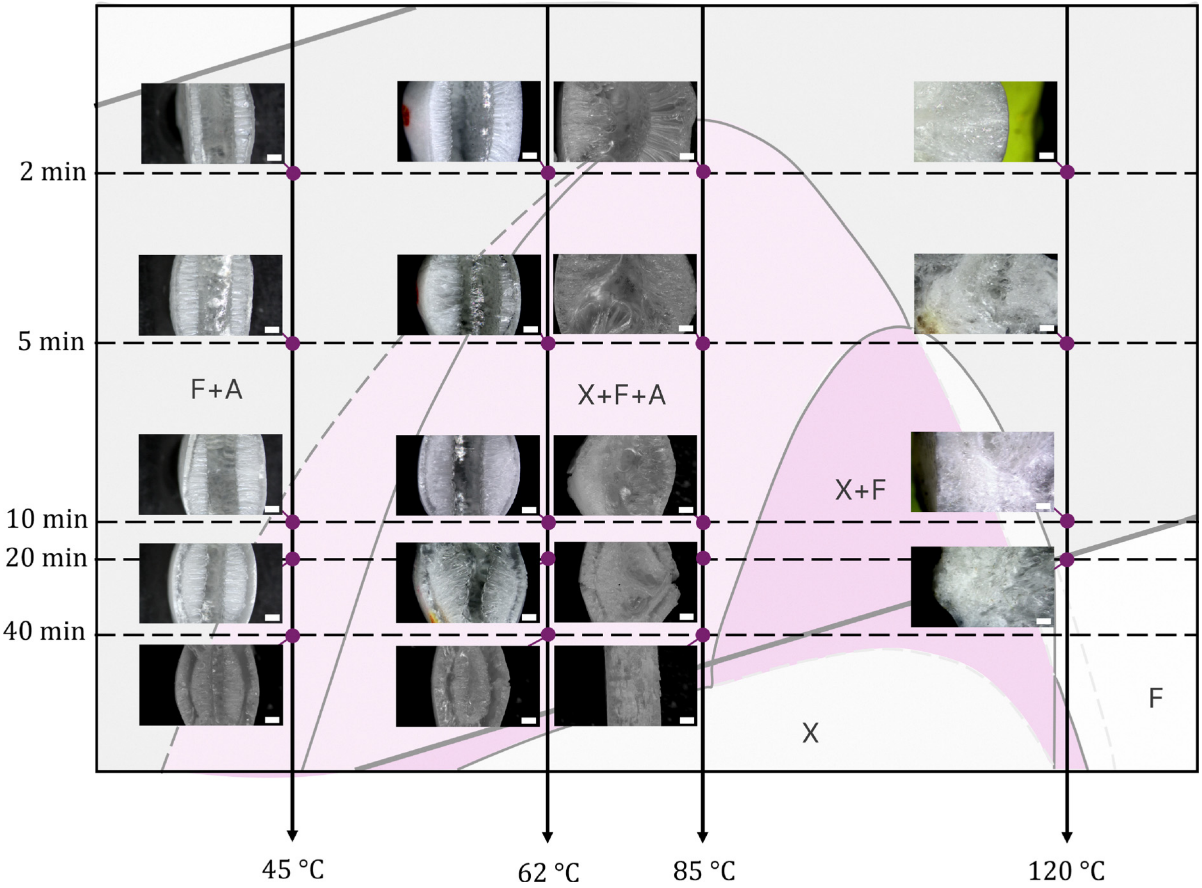

Fig. 4 Microscopy images of the cross sections of the PLLA samples (L = 1 mm) treated with 110 bar of CO_2 at T = 45, 62, 85 and 120 °C for a time t_p = 2, 5, 10, 20 and 40 min superimposed on the zoomed-in TTTL diagram. The additional dashed grey curve was added to take into account the fact that we used a higher pressure value for foaming with respect to that found in the literature (45 bar). Concerning the samples treated at 120 °C for 2 and 5 min, we decided to only show the foamed part as the samples in their entirety were much larger than the field of view of the optical microscope and it was not possible to include both the amorphous and foamed layers in just one microphotograph. Scale bar = 500 μm.

processing conditions, together with the optical micrographs of the cross sections of the resulting samples, are shown in Fig. 4. These are directly overlaid on the zoomed-in TTTL diagram to demonstrate the analogy between expected and experimental results. As visible, a good correspondence can be found at T = 62, 85 and 120 °C for all processing times, as the three-layered structure only appears in the light pink region (X + F + A). Conversely, when outside of it (dark grey region), only two-layers are visible, as the conditions to initiate crystallization are not yet met. Some discrepancies are found only in the samples treated at T = 45 °C, specifically for longer processing times (t_p = 10, 20, and 40 min). This is likely due to the fact that the high pressure crystallization kinetics were retrieved from literature data collected at 45 bar of CO_2, while our experiments were conducted with 110 bar of CO_2, a much higher value. As already discussed, the actual crystallization kinetics at such a high pressure is even more shifted toward lower temperature values, and the (X + F + A) region can be extended accordingly, as exemplified in Fig. 4 by the grey dashed curve.[18]

As a final remark, scale-up was successfully performed. Indeed, to prove the beneficial effect of layering on mechanical performance, we produced PLLA slabs with a geometry suitable for three point bending tests (18 × 2 × 100 mm^3 in dimensions). The resulting samples and the corresponding optical and POM microphotographs are shown in Fig. 5. Regarding the mechanical properties, with respect to the totally crystalline beam (X), the (X + F + A) sandwich showed a slight reduction in bending stiffness (−12%) but a remarkable increase in fracture energy (+210%), due to the presence of the tougher amorphous and foamed core (Fig. 5c). The possibility of improving performance in a single-material, sustainable part was thus demonstrated.

This very interesting and promising result lays the foundation for a new approach to batch foaming, not only of PLLA but also of any semi-crystalline polymer. An example of how the TTTL diagram can appear in the case of PET is shown in Fig. 6, where literature data[19,45,48,54–60] on thermal and mass diffusivities, as well as on PET crystallization under CO_2, are compared to assess the feasibility of designing treatments for material layering, similarly to what was done for PLLA. The corresponding TTTL diagram for a slab of the polymer with L = 1 mm is presented in Fig. 6b, highlighting a completely different picture, as new challenges and possibilities arise when changing the polymer.

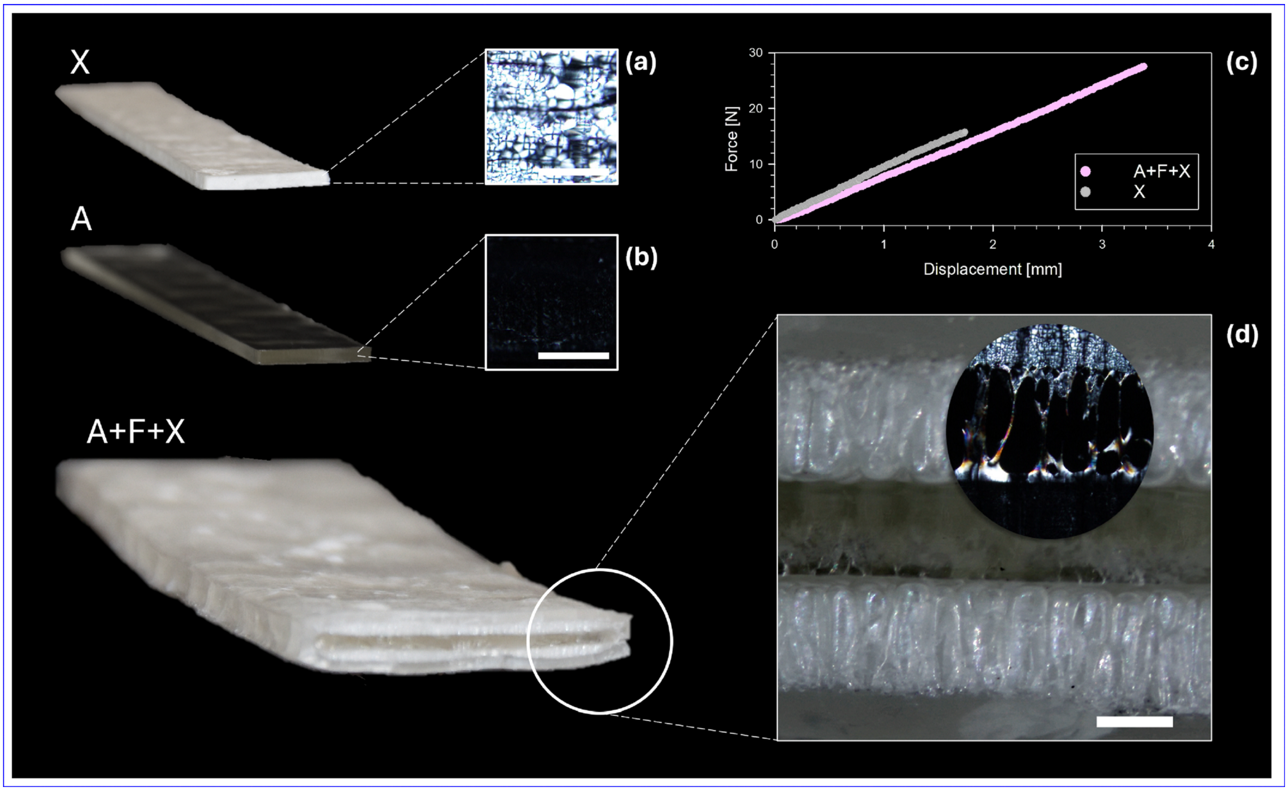

Fig. 5 Crystalline (X), amorphous (A), and layered (X + F + A) PLLA slabs produced for the three point bending tests through scale up of the already presented process. The corresponding POM micrographs, (a), (b) and (d), respectively, are also presented. Scale bar = 200 μm in (a) and (b), and 500 μm in (d). The force–displacement curves resulting from the three point bending tests on the scaled up crystalline (X) and layered (A + F + X) samples are shown in (c).

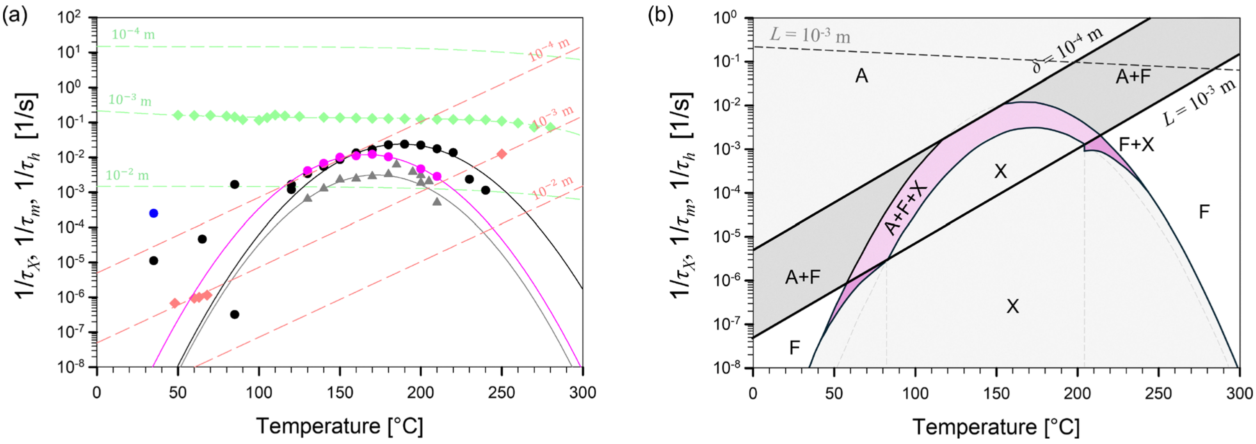

Fig. 6 (a) Comparison of the rates of the three concurring phenomena for the system PET/CO$_2$. $1/\tau_m = D/L^2$ (light red diamonds) is the rate of mass transport[48,54–56] $1/\tau_h = a/L^2$ (green diamonds) is the rate of heat transport;[57] $1/\tau_X$ is the crystallization rate. The latter is presented as a function of CO$_2$ pressure: black, dark blue and blue circles indicate $1/\tau_X$ at ambient pressure,[58,59] with 50 bar of CO$_2$[58] and with 60 bar of CO$_2$,[45] respectively, in the case of cold crystallization; similarly, grey and pink triangles indicate $1/\tau_X$ at ambient pressure[19,60] and with 60 bar of CO$_2$[60] in the case of melt crystallization. A value of L = 0.1, 1 and 10 mm was used for the evaluation of $1/\tau_m$ (dashed red lines) and $1/\tau_h$ (dashed green lines). (b) TTTL diagram for a slab of PET (L = 1 mm) treated with CO$_2$. The superimposition of the kinetic curves evidences the presence of six different regions: amorphous (A, light grey), crystalline (X, grey), foamed (F, white), two-layered foamed–amorphous structure (A + F, dark grey), two-layered foamed–crystalline structure (F + X, dark pink) and three layered foamed–amorphous–crystalline structure (A + F + X, pink). In this case, the heat transport curve is also evidenced (dashed light grey line).

It is evident that, in this instance, the possibility of obtaining a layered structure still exists; however, due to the less effective CO$_2$ plasticizing effect, much smaller (X + F) and (X + F + A) regions are identified, implying a higher intrinsic difficulty in

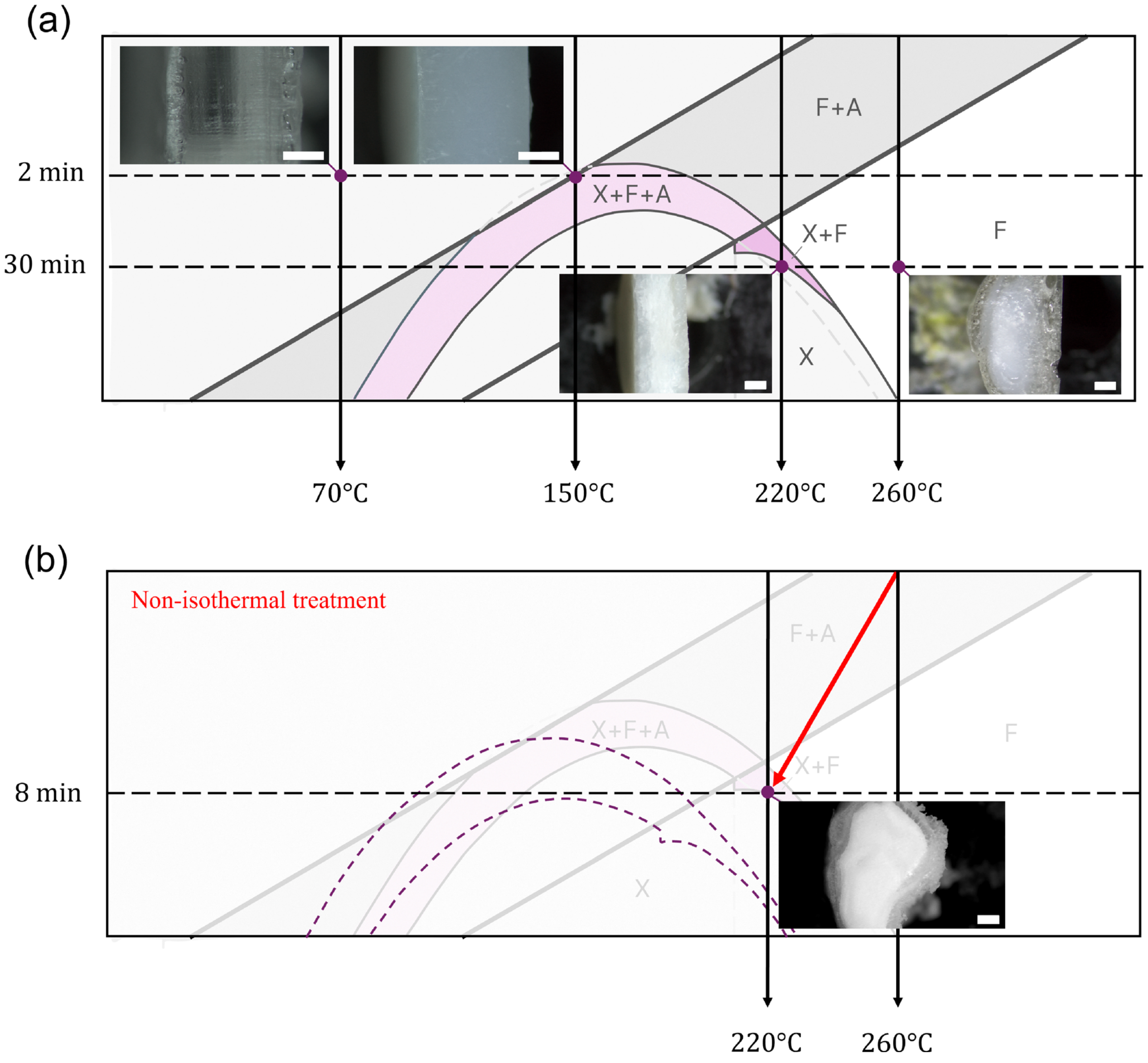

Fig. 7 (a) Optical micrographs of the cross sections of the PET samples (L = 1 mm) treated with 110 bar of CO_2 (a) at a constant temperature of 70, 150, 220 and 260 °C for a time t_p = 2 and 30 min and (b) under continuous cooling from 260 to 220 °C for a time t_p = 8 min. In (b), a shift in the bell-shaped crystallization curves as a consequence of the non-isothermal treatment is also qualitatively presented (dashed purple lines). Scale bar = 500 μm in both (a) and (b).

the layering of PET through isothermal treatments in comparison to PLLA.

This is also evident from Fig. 7a, where similar to Fig. 4, the optical micrographs of the cross sections of processed PET slabs (L = 1 mm) are overlaid on the corresponding zoomed-in TTTL diagram. Here, despite the proximity of the adopted experimental conditions to the (X + F + A) and (X + F) regions, we were never able to obtain a layered sample; indeed, only fully amorphous, crystalline, and foamed samples are shown.

Nevertheless, new methods to induce layering can be attempted, considering the new picture at hand. Going back to Fig. 6a, a higher rate of heat transport can be observed, with a curve that is visibly closer to both the diffusion and crystallization lines. This non-trivial observation allows us to consider the implementation of thermal treatments as an additional means to obtain layering in PET.

A first attempt at this approach is shown in Fig. 7b, where the continuous cooling of the PET slab is considered (red arrow). As a consequence of the non-isothermal treatment, the isothermal transformation (TTTL) diagram is no longer valid, and a shift in the crystallization curves must be considered; indeed, the time required for crystallization to occur is delayed during continuous cooling, and the corresponding bell-shaped lines are shifted to longer times and lower temperatures (dashed purple lines).[61] The optical micrograph of the cross section of the resulting sample is superimposed on the qualitatively modified graph and shows the effectiveness of this treatment, as a two-layer structure appears. However, a careful and thorough re-thinking of the TTTL diagrams must be considered when dealing with non-isothermal treatments (similarly to what happens in the continuous cooling transformation – CCT – diagrams[61]), to guaranty full comprehension and accurate representation of these processes.

The implementation of this technique is applicable to any type of material processing where a layering within a certain depth δ is desired, as long as the following criteria are met: (i) the process involves the transport of mass, momentum, and/or energy (characterized, through δ, by a rate $1/\tau_{tr}$); (ii) the process involves a transformation (characterized by a rate $1/\tau_X$), affected by the transported quantities; (iii) there exists a condition for which $Da_\delta = \tau_{tr}/\tau_X \approx 1$.

Once the potential for layering is established and all the required criteria are met, the TTTL diagram for the system at hand can be built. Starting from the kinetic data for both the transformation and transport phenomena, the evaluation of τ_{tr} and τ_X as a function of processing conditions can be exploited to highlight the precise processing window needed to achieve a target layering. The final step requires validation of the theoretically built diagram through a thorough experimental campaign.

4 Conclusions

In the present work, we introduce a novel technique to induce material layering in semi-crystalline polymers, specifically referring to the cases of poly(lactic acid) (PLLA) and polyethylene terephthalate (PET). We demonstrate that knowledge of the interplay between the numerous transport phenomena happening during physical foaming of a semi-crystalline polymer (heat transport, mass transport and crystallization) is a powerful tool to tailor both foam density and crystallinity distributions in mono-material polymer systems within a single processing step.

Literature data on mass diffusivity, thermal diffusivity and crystallization kinetics of the PLLA/CO_2 and PET/CO_2 systems are explored and a more intuitive way of understanding the processing conditions is provided, in which semi-crystalline polymers can give rise to a layered structure in the laboratory practice of batch foaming. Specifically, the time–temperature–transformation-layering (TTTL) diagram is presented, with experimental results confirming its effectiveness in predicting the final sample morphology. With this tool at hand, multilayered foams are obtained, presenting, in the best cases, an amorphous core, a foamed part, and a crystalline skin. The potential of using such graph in any type of material processing in which layering is desired is also foreseen, and the operational pathway to be followed when approaching a new material system is also provided. In this way, the proposed methodology establishes itself as a fully generalizable framework for processing-driven material structuring.

Future developments may focus on extending the concept to other classes of polymers and reactive systems and to other classes of materials (*e.g.*, metals where time–temperature–transformation diagrams are used, and layering is also a frequent need), further bridging the gap between performance optimization and circular design principles.

Author contributions

Emilia Di Lorenzo: writing – original draft, writing – review & editing, validation, methodology, investigation, formal analysis, data curation, conceptualization, visualization. Lorenzo Miele: writing – original draft, writing – review & editing, validation, methodology, investigation, formal analysis, data curation, conceptualization, visualization. Alessandra Longo: writing – review & editing, conceptualization, investigation, project administration, resources. Ernesto Di Maio: writing – original draft, writing – review & editing, conceptualization, funding acquisition, project administration, supervision, resources. Maria Laura Di Lorenzo: writing – review & editing, conceptualization, project administration, funding acquisition, supervision, resources.

Conflicts of interest

The authors declare no competing interests.

Data availability

The data that support the findings of this study are openly available on figshare, https://figshare.com/s/b1b75594bf0fd1a3adae.

Acknowledgements

This research was funded by the European Union-Next Generation EU-PNRR M4/C2/INVESTIMENTO.1.1, in the framework of the PRIN 2022 PNRR program (D.D. 1409, 14-9-2022), project n.P20229YNXX ''Design for Recyclability: mono-material multigraded semicrystalline polymer foams'' (DesiRe), ERC field PE11, CUP B53D23027510001. The authors thank Costantino Casale (University of Naples Federico II) for the support provided in performing polarized optical microscopy (Fig. 2 and 5), Arsenio Cutolo (University of Naples Federico II) for atomic force microscopy (Fig. 2), and Antonio Langella and Massimo Durante (University of Naples Federico II) for the mechanical test. The authors also warmly thank Total Corbion (Gorinchem, the Netherlands) and Point Plastic (Amasona, Italy) for kindly providing PLLA and PET, respectively.

Notes and references

1 J. Wiener, F. Arbeiter, O. Kolednik and G. Pinter, *Mater. Des.*, 2022, **219**, 110828.
2 T. Magrini, A. Senol, R. Style, F. Bouville and A. R. Studart, *J. Mech. Phys. Solids*, 2022, **159**, 104750.
3 A. R. Alias, M. K. Wan and N. Sarbon, *Food Control*, 2022, **136**, 108875.

4 R. O. Ritchie, *Nat. Mater.*, 2011, **10**, 817–822.

5 A. Kausar, I. Ahmad, S. A. Rakha, M. Eisa and A. Diallo, *J. Compos. Sci.*, 2023, **7**, 102.

6 J.-P. Lange, *ACS Sustainable Chem. Eng.*, 2021, **9**, 15722–15738.

7 L. Shen and E. Worrell, *Handbook of recycling*, Elsevier, 2024, pp. 497–510.

8 K. Ragaert, S. Huysveld, G. Vyncke, S. Hubo, L. Veelaert, J. Dewulf and E. Du Bois, *Resour., Conserv. Recycl.*, 2020, **155**, 104646.

9 M. Guerritore, F. Olivieri, R. Castaldo, R. Avolio, M. Cocca, M. E. Errico, M. R. Galdi, C. Carfagna and G. Gentile, *Resour., Conserv. Recycl.*, 2022, **179**, 106126.

10 P. Iaccarino, E. Maresca, S. Morganti, F. Auricchio and E. Di Maio, *Adv. Eng. Mater.*, 2024, **26**, 2301798.

11 J. Zhao, L. Zhang, J. U. Lee, N. D. Sansone, J. Kim, L. Bazbaz, A. A. Faysal and P. C. Lee, *Small*, 2025, **21**, e08472.

12 Q. Cheng, L. Jiang and Z. Tang, *Acc. Chem. Res.*, 2014, **47**, 1256–1266.

13 M. Trofa, E. Di Maio and P. L. Maffettone, *Chem. Eng. J.*, 2019, **362**, 812–817.

14 E. Di Lorenzo, F. Romano, L. Ciriaco, N. Iaccarino, L. Izzo, A. Randazzo, P. Musto and E. Di Maio, *Commun. Eng.*, 2025, **4**, 1–10.

15 E. Di Lorenzo, R. Pasquino, N. Grizzuti and E. Di Maio, *Phys. Fluids*, 2025, **37**(2), 023145.

16 D. Tammaro, V. Contaldi, M. P. Carbone, E. Di Maio and S. Iannace, *J. Cell. Plast.*, 2016, **52**, 533–543.

17 L. Miele, E. Di Lorenzo, C. Guissart and E. Di Maio, *Heliyon*, 2024, **10**(12), e32420.

18 A. Longo, E. Di Maio and M. L. Di Lorenzo, *Thermochim. Acta*, 2022, **718**, 179386.

19 M. L. Di Lorenzo, *Polymers*, 2024, **16**, 1975.

20 A. Longo, E. Di Maio, F. Du, R. Androsch and M. L. Di Lorenzo, *Polymer*, 2023, **285**, 126380.

21 M. L. Di Lorenzo, *Macromol. Symp.*, 2006, **234**, 176–183.

22 M. L. Di Lorenzo, *J. Appl. Polym. Sci.*, 2006, **100**, 3145–3151.

23 M. L. Di Lorenzo and R. Androsch, Crystallization of Poly(lactic acid), in *Biodegradable Polyesters*, ed. S. Fakirov, 2015.

24 M. L. Di Lorenzo and R. Androsch, *Macromol. Chem. Phys.*, 2016, **217**, 1534–1538.

25 P. Trucillo, F. Errichiello and E. Di Maio, *J. Appl. Polym. Sci.*, 2023, **140**, e54574.

26 G. Li, H. Li, L. Turng, S. Gong and C. Zhang, *Fluid Phase Equilib.*, 2006, **246**, 158–166.

27 H. Sawada, Y. Takahashi, S. Miyata, S. Kanehashi, S. Sato and K. Nagai, *Trans. Mater. Res. Soc. Jpn.*, 2010, **35**, 241–246.

28 K. Yu, H. Zhou, X. Wang, Z. Du and J. Mi, *J. Mol. Liq.*, 2019, **280**, 97–103.

29 E. Aionicesei, M. Škerget and Ž. Knez, *J. Supercrit. Fluids*, 2008, **47**, 296–301.

30 L. Bai, X. Zhao, R.-Y. Bao, Z.-Y. Liu, M.-B. Yang and W. Yang, *J. Mater. Sci.*, 2018, **53**, 10543–10553.

31 M. Nofar, W. Zhu and C. Park, *Polymer*, 2012, **53**, 3341–3353.

32 H. Tsuji, H. Takai and S. K. Saha, *Polymer*, 2006, **47**, 3826–3837.

33 M. Day, A. Nawaby and X. Liao, *J. Therm. Anal. Calorim.*, 2006, **86**, 623–629.

34 A. Fernández-Tena, M. Fernández, A. J. Sandoval, M. I. Calafel, A. Aguirre, N. Aranburu, G. Guerrica-Echevarria, M. L. Di Lorenzo, A. Longo and J. F. Vega, *et al.*, *Int. J. Biol. Macromol.*, 2024, **282**, 136783.

35 L. Yu, H. Liu, K. Dean and L. Chen, *J. Polym. Sci., Part B: Polym. Phys.*, 2008, **46**, 2630–2636.

36 A. Longo, E. Di Lorenzo, L. Miele, A. Bernardi, E. Di Maio and M. L. Di Lorenzo, *J. Polym. Environ.*, 2026, **34**, 90.

37 G. Federico, A. R. Carotenuto, A. Cutolo, M. Fraldi and F. Carlomagno, *Sci. Rep.*, 2025, **15**, 18037.

38 M. L. Di Lorenzo, P. Rubino, R. Luijkx and M. Hélou, *Colloid Polym. Sci.*, 2014, **292**, 399–409.

39 M. L. Di Lorenzo, P. Rubino, B. Immirzi, R. Luijkx, M. Hélou and R. Androsch, *Colloid Polym. Sci.*, 2015, **293**, 2459–2467.

40 R. Androsch, M. L. Di Lorenzo and C. Schick, *Eur. Polym. J.*, 2017, **96**, 361–369.

41 R. Androsch, C. Schick and M. L. Di Lorenzo, *Adv. Polym. Sci.*, 2017, **279**, 235–272.

42 M. Nofar, A. Tabatabaei and C. B. Park, *Polymer*, 2013, **54**, 2382–2391.

43 M. Nofar, A. Tabatabaei, A. Ameli and C. B. Park, *Polymer*, 2013, **54**, 6471–6478.

44 D.-C. Li, T. Liu, L. Zhao, X.-S. Lian and W.-K. Yuan, *Ind. Eng. Chem. Res.*, 2011, **50**, 1997–2007.

45 S. Lambert and M. Paulaitis, *J. Supercrit. Fluids*, 1991, **4**, 15–23.

46 S. Kadijk and B. Van Den Brule, *Polym. Eng. Sci.*, 1994, **34**, 1535–1546.

47 P. Condo, I. C. Sanchez, C. Panayiotou and K. P. Johnston, *Macromolecules*, 1992, **25**, 6119–6127.

48 J. Chiou, J. W. Barlow and D. R. Paul, *J. Appl. Polym. Sci.*, 1985, **30**, 2633–2642.

49 R. Pantani, V. Speranza and G. Titomanlio, *Eur. Polym. J.*, 2017, **97**, 220–229.

50 J. Magill, *J. Mater. Sci.*, 2001, **36**, 3143–3164.

51 R. Aguiar, N. D. Sansone, N. Cheung, A. V. Tuccitto, T. Y. T. Su, I. Soltani, M. Leroux and P. C. Lee, *Adv. Funct. Mater.*, 2024, **34**, 2403728.

52 D. E. Martnez-Tong, A. Najar, M. Soccio, A. Nogales, N. Bitinis, M. López-Manchado and T. Ezquerra, *Compos. Sci. Technol.*, 2014, **104**, 34–39.

53 G. Molinari, P. Parlanti, L. Aliotta, A. Lazzeri and M. Gemmi, *Mater. Today Commun.*, 2024, **38**, 107868.

54 A. S. Michaels, W. R. Vieth and J. A. Barrie, *J. Appl. Phys.*, 1963, **34**, 13–20.

55 W. J. Koros and D. R. Paul, *Polym. Eng. Sci.*, 1980, **20**, 14–19.

56 L. Sorrentino, E. Di Maio and S. Iannace, *J. Appl. Polym. Sci.*, 2010, **116**, 27–35.

57 J. Morikawa and T. Hashimoto, *Polymer*, 1997, **38**, 5397–5400.

58 K. Mizoguchi, T. Hirose, Y. Naito and Y. Kamiya, *Polymer*, 1987, **28**, 1298–1302.

59 J. Jog, *J. Macromol. Sci., Part C: Polym. Rev.*, 1995, **35**, 531–553.

60 M. Takada and M. Ohshima, *Polym. Eng. Sci.*, 2003, **43**, 479–489.

61 W. D. Callister and D. G. Rethwisch, *Fundamentals of materials science and engineering*, John Wiley & Sons, 2022.